

Plasmonic Tipless Pyramid Arrays for Cell Poration

Sébastien Courvoisier,^{*,†,‡} Nabih Saklayen,[‡] Marinus Huber,[‡] Jun Chen,^{‡,⊥} Eric D. Diebold,^{‡,§} Luigi Bonacina,[†] Jean-Pierre Wolf,^{*,†} and Eric Mazur^{*,‡}

[†]Group of Applied Physics, Biophotonics Group, University of Geneva, 22 chemin de Pinchat, 1227 Carouge, Switzerland

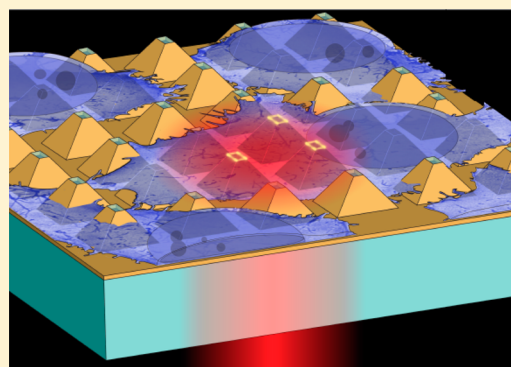
[‡]Department of Physics and School of Engineering and Applied Sciences, Harvard University, 9 Oxford Street, Cambridge, Massachusetts 02138, United States

[§]Department of Electrical Engineering, California NanoSystems Institute, UCLA, Los Angeles, California 90095, United States

[⊥]School of Materials Science and Engineering, Nanjing University of Science and Technology, Nanjing 210094, People's Republic of China

S Supporting Information

ABSTRACT: Improving the efficiency, cell survival, and throughput of methods to modify and control the genetic expression of cells is of great benefit to biology and medicine. We investigate, both computationally and experimentally, a nanostructured substrate made of tipless pyramids for plasmonic-induced transfection. By optimizing the geometrical parameters for an excitation wavelength of 800 nm, we demonstrate a 100-fold intensity enhancement of the electric near field at the cell–substrate contact area, while the low absorption typical for gold is maintained. We demonstrate that such a substrate can induce transient poration of cells by a purely optically induced process.



KEYWORDS: Cell transfection, plasmonics, ultrafast laser, nanostructured substrate, tipless pyramid, nanophotonics

Plasmonic nanostructured substrates have recently emerged as attractive alternatives to deposited nanoparticles for applications such as label-free bio sensing, surface enhanced Raman scattering (SERS) spectroscopy, and nanometric sized particle trapping.^{1,2} In particular, nanopyramids have attracted much attention because they provide large-field enhancement in a very confined and well-defined volume at the tip^{3,4} enabling, among others, near-field imaging and spectroscopy.⁵ Moreover, their relatively easy fabrication based on template-stripping opens up the possibility of large-scale production.

Plasmonic nanostructures, such as gold nanoparticles, have been used for inducing transient poration of cell membranes, allowing neighboring molecules (such as genetic material in the case of transfection) to enter the cell. Compared to other methods, such as electroporation, plasmonic transfection is spatially selective and shows a better cell viability.⁶ The first experiments on laser-induced plasmonic transfection were conducted using gold nanoparticles as strong near-field light scattering centers.⁷ More recently, a transfection efficiency of about 25% and cell viability of 80% were achieved using an off-resonance nanoparticles plasmonic setup.⁸ Likewise, transfection efficacy (75%) and viability (84% at 48 h) were achieved by plasmon-induced cavitation bubbles.⁶ The plasmonic bubbles are created by irradiating gold nanoparticle clusters selectively attached on cell membranes by covalently bound antibodies. However, plasmonic transfection using gold

nanoparticles raises the issue of possible nanoparticle toxicity.⁹ Gold nanoparticle incorporation in cells might induce oxidative stress, which can lead to DNA damage and cause autophagy as a cell survival response behavior.¹⁰

Inspired by the results achieved with gold nanoparticles, we developed and designed nanostructured substrates that show a high localized and controlled near-field enhancement while minimizing the nanoparticle residues left in the cells. The localized field enhancement is expected to contribute to achieving high-throughput, efficient, and low toxicity opto-plasmonic transfection. Our plasmonic nanostructures consist of tipless pyramids (Figure 1a), which combine the plasmonic enhancement of the pyramid shape and the advantages of nanoapertures.^{11,12} Illumination of the pyramidal nanostructured metal substrate with a femtosecond laser excites surface plasmons that strongly enhance the field at the nanoscale aperture of the pyramid. These strong local fields can induce photoionization and plasma formation.¹⁴ Subsequent thermalization in the medium leads to the formation of vapor bubbles and pressure waves. We expect these plasma-mediated bubbles to play a major role in the poration and transfection of cells.¹² The poration is followed by the subsequent uptake of the

Received: March 2, 2015

Revised: June 13, 2015

Published: June 16, 2015

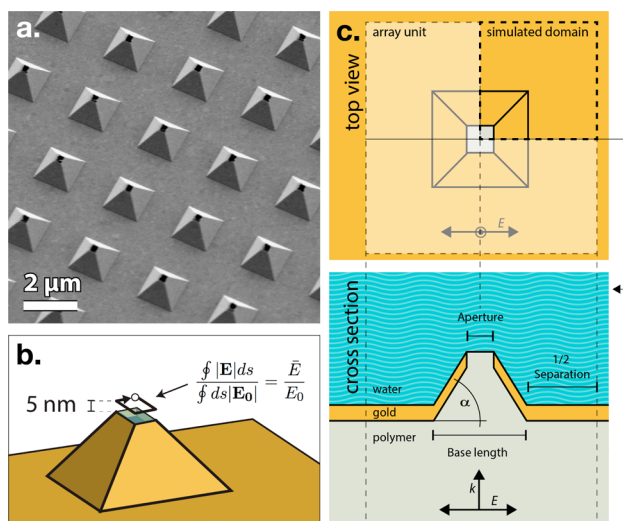


Figure 1. (a) Scanning electron microscopy image of a tipless pyramid array; (b, c) schematic diagram of a tipless pyramid and field enhancement figure of merit used in simulation.

transfection material by the cell. The use of femtosecond excitation has the advantage of reducing thermal damage both for cells and substrate.^{13,14}

The nanofabrication of the substrate was performed in a cleanroom facility to avoid any unwanted contamination and defects. First, an accurate inverted array of squares on a silicon (Si) wafer is produced by e-beam lithography. The unmasked areas of the Si wafer are then anisotropically wet-etched with potassium hydroxide (KOH). The differential etching rate of the various Si crystalline axes produces perfectly smooth surfaces and sharp-edged pyramidal divots by revealing the slowly etching (111) planes of the crystal.¹⁵ The resulting template is then placed on a tilted rotary stage at a specific angle in a high vacuum deposition chamber. While the stage rotates, gold is thermally evaporated on the template to create a 40-nm thin gold layer. The base edges of each divot cast a shadow at the bottom of the divot, which results in an aperture at the tip of the pyramid.¹⁶ The resulting bottomless gold layer divots are attached on a glass slide by optical grade UV curable glue and then lifted off revealing the pyramid array covered by a tipless gold thin film. The resulting nanostructure consists of an array of tipless pyramids whose geometrical parameters are pyramids' base length, aperture size, separation distance between pyramids, and gold thickness (Figure 1c). The aperture is linearly dependent on the base length due to the gold deposition angle during the fabrication process.

We assessed the geometrical parameters and surface quality of fabricated samples by optical microscopy and scanning electron microscopy (SEM). The cross-sectional quality and gold thickness on the pyramid sidewalls were measured on selected samples under SEM after milling by focused ion beam (FIB).

Figure 1, panel a shows the SEM image of a substrate. The FIB cross-sectional measurement under SEM reveals a gold thickness of 40 ± 5 nm on the separation surface and 30 ± 5 nm on the pyramids sidewalls (not shown). The nanofabrication process makes it possible to maintain a fabrication tolerance below 10 nm for the base length, separation distance, and aperture within one fabrication batch. The high level of control in the fabrication process allows us to prepare sets of arrays with controlled parameters variations (see Figure 2a).

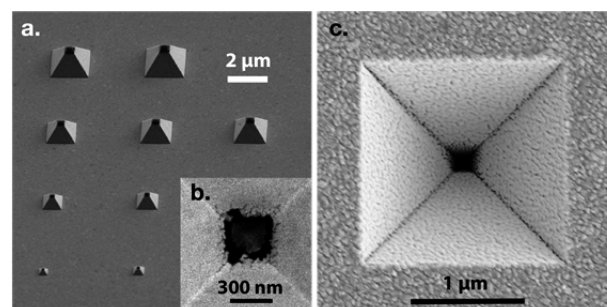


Figure 2. Scanning electron microscopy. (a) Pyramids of varying size show the high precision of the fabrication process and the linear dependence of the aperture on the base length for a given deposition angle; (b) close top view of a pyramid aperture; (c) top view of a Si wafer template with the deposited thin gold layer before the lift-off process.

The major fabrication limitation is associated with the gold thermal evaporation process, which limits the aperture sharpness (Figure 2b) and the gold roughness inside the pyramid (Figure 2c).

To probe the electric field enhancement produced at the tipless pyramids, we used a near-field scanning optical microscope (NSOM) with a 80-nm aperture probe. For these measurements, the pyramid array was excited from the backside with a 780 nm continuous wave laser in collection mode. In a second set of experiments, we probed the localization of the nonlinear field enhancement by imaging the second harmonic (SH) emission from the nanostructures using a multiphoton microscope (Nikon A1R-Multiphoton). In this case, a femtosecond Ti:sapphire oscillator at 790 nm was used as excitation laser, and the substrate was immersed in water to closely match the application conditions.

To find the optimal geometrical parameters of the pyramid arrays, two complementary simulation methods were used: finite-difference time-domain simulation (FDTD Solutions v8.6 from Lumerical) and finite element method (FEM, COMSOL multiphysics v4.3b). The former method was used to understand the temporal behavior of excited surface plasmon polaritons and the second method for exploring the geometrical parameter space of the pyramids array, as FEM is more robust against numerical artifacts during geometrical parameter sweeps.¹⁷ In both cases, periodic and antiperiodic boundary conditions were applied in the x and y directions to exploit the symmetry of the system. For FDTD, the optical input was defined as a linearly polarized plane wave with a temporal envelope of 45 fs full width at half maximum (fwhm) centered at a wavelength of 800 nm. In the vicinity of the nanoaperture, the maximum size of the mesh was set to 3 nm. FEM simulations were carried out in the frequency-domain using an 800-nm plane wave excitation source, and all sharp edges were rounded with a 5-nm radius.

The top left panel of Figure 3 shows one example of the obtained NSOM photon-count image, indicating enhanced emission localized primarily at the edges of the pyramid's aperture. The concentric modulation pattern around the central area can be understood in terms of the nodes of a standing wave of plasmonic excitation along the pyramid's sides. The corresponding FEM results in the adjacent panel confirm the localization of the plasmonic enhancement pattern at the aperture in good agreement with the experimental observation. The calculations also account for the presence of concentric,

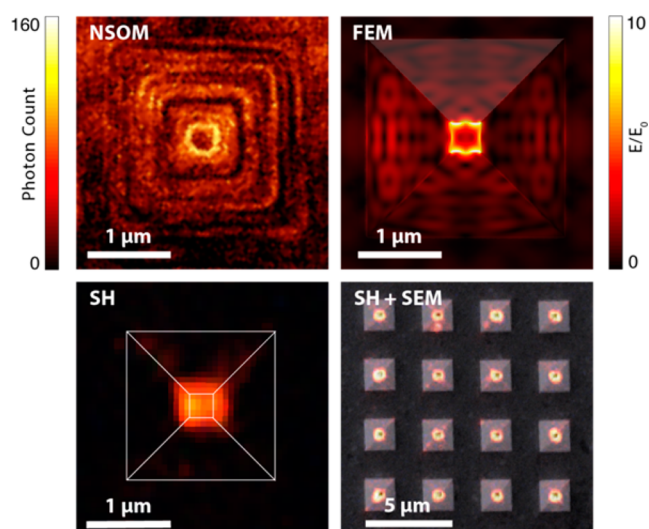


Figure 3. NSOM photon count image of a pyramid; FEM simulation results for the corresponding geometry (E/E_0 projection); SH maximal intensity projection (white lines: outline of the pyramid). SH+SEM: overlay of SH and SEM images of a pyramid array.

weaker modulations. Further details on the onset of the excitation are provided in the time-resolved cross-section enhancement animation found in the Supporting Information. Overall, the simulations accurately capture the pyramid response to linear laser excitation. The smeared pattern in the experimental photon-counting level image is likely due to the interplay between the roughness of the gold layer and the finite dimension of the NSOM scanning tip (80 nm). Simulations also show that laser polarization affects the localization of the enhancement along the aperture edges but does not significantly influence its intensity (data not shown).

An alternative way to experimentally probe local-field enhancement is detecting the efficiency of parametric nonlinear processes by SH microscopy.¹⁸ In the bottom left panel of Figure 3, we present the maximum intensity projection of a three-dimensional SH-intensity scan. We observe that the SH emission is strongly localized at the tipless aperture area. When the SH emission is compared with the field-enhancement simulation in the FEM plot, one must take into account the different intensity dependences (SH scales as I^2) and the limited spatial resolution (several hundreds of nanometers), which limit the possibility of capturing the enhancement along the edges of the aperture and the modulations along pyramids' sides. In the bottom right panel of Figure 3, the second harmonic emission is superimposed on the SEM image of a substrate, showing the spatial uniformity of the emission throughout the array.

To optimize the substrates, we carried out a thorough numerical investigation of the dependence of the electric field at the aperture on the geometrical parameters (separation distance between pyramids, base length, and aperture size). We define an appropriate figure of merit as the average local E-field enhancement 5 nm above the aperture for an excitation at 800 nm. This definition of the figure of merit is supported by several arguments. The choice of limiting the computation to the aperture is in line with the results of the SH, NSOM, and simulation results in Figure 3, indicating that the enhancement occurs essentially along the aperture edges. The line average is independent of the aperture size. Also, the 5 nm distance is

within the range of the minimal substrate–membrane separation.¹⁹

Figure 4 shows the calculated local enhancement as a function of the separation distance. The aperture was set to 290

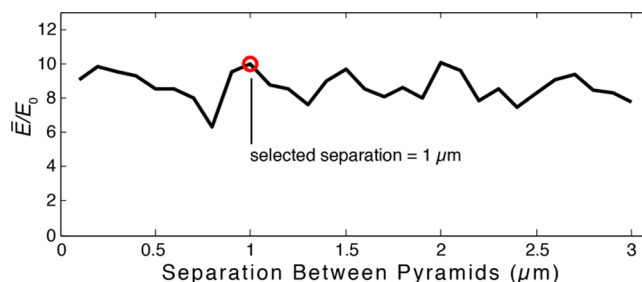


Figure 4. Dependence of the local enhancement figure of merit on the separation distance between pyramids.

nm and the baselength to 2.2 μm . These values correspond to high enhancement in our numerical model (region of interest 2, Figure 5). The separation distance sweep exhibits several local

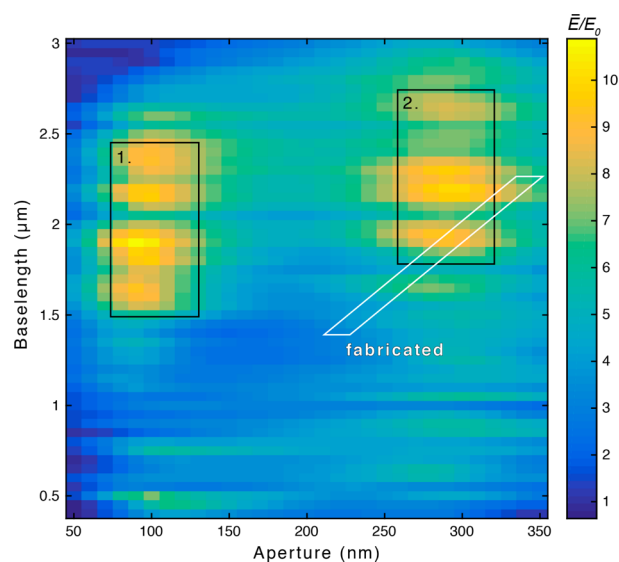


Figure 5. Simulated local enhancement as a function of both aperture and base length of the tipless pyramids. Rectangles 1 and 2: high enhancement parameters regions. The white outline indicates the fabricated pyramid arrays used in SH measurements.

maxima with similar enhancements, indicating that the separation between pyramids influences weakly the overall near-field enhancement over the investigated range (0.1–3 μm). This crosstalk can be attributed to surface plasmon coupling between the pyramids sidewalls through surface plasmon polariton traveling along separation surfaces. Calculations show that on the time scale of the laser excitation surface plasmon waves reach neighboring pyramids and interfere with each other (see Supporting Information). The described crosstalk behavior will allow us to change the number of pyramids per area while maintaining a high field enhancement. This can be useful in cell manipulation experiments by controlling the number of pyramids per cell to maximize cell viability and poration efficiency. For example a 1- μm interpyramid separation distance with a 2.2- μm base length

yields a spot density of approximately $10^7/\text{cm}^2$, corresponding to roughly 30 pyramids for a $20\text{ }\mu\text{m}$ diameter cell.

On the other hand, the dependence of the electric field at the aperture on the geometrical parameters of the individual pyramids is significant. Figure 5 shows the enhancement figure of merit as a function of aperture size and pyramid base length. We identified two regions associated with high enhancement (see. Figure 5). Pyramids in region 1 have an aperture of about 100 nm and base length range of $1.5\text{--}2.5\text{ }\mu\text{m}$. Region 2 corresponds to an aperture of 300 nm and base length spanning between 1.75 and $2.5\text{ }\mu\text{m}$. The second region allows easier fabrication. The observed base length dependence can be explained by the buildup of quasi standing waves along pyramid faces. Strong enhancements appear when the base length allows standing waves antinodes on the pyramid faces to match the aperture edges. The strong field enhancement of 100 and 300 nm apertures can be explained by the buildup of dipolar (Figure 6a) and quadrupolar (Figure 6b) resonant modes,

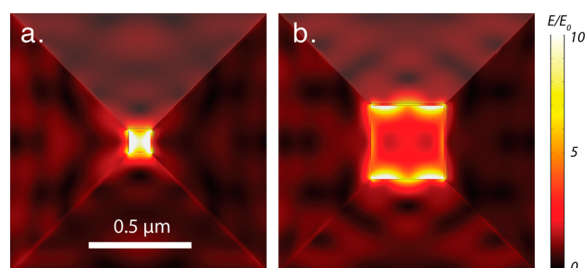


Figure 6. FEM simulation, enhancement projection, top view of the pyramid aperture: (a) 120-nm aperture; (b) 310-nm aperture.

respectively. Overall, calculations indicate that one can expect a 100-fold enhancement of the input optical electric field intensity in the aperture region.

In Figure 7, the high reflectance and low absorptance and transmittance at 800 nm shown in the left panel suggest that

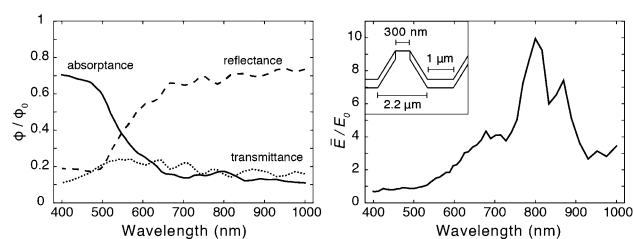


Figure 7. FEM simulation of pyramid with aperture, 300 nm ; base length, $2.2\text{-}\mu\text{m}$; separation distance, $1\text{ }\mu\text{m}$; and gold thickness, 50 nm . Left panel: spectral absorptance, reflectance, and transmittance. Right panel: local enhancement at the aperture; inset, cross-section schematic of the selected geometry.

even the structure was optimized for the highest field enhancement at this wavelength (right panel); we keep the low absorption typical for a gold film at this wavelength. This combined low absorptance regime and optimally enhanced near field at the aperture allow a better energy transfer to the surrounding medium (water) while minimizing thermal damage to the tipless pyramid substrate.

In Figure 8, we compare the SH intensity measurement with the calculated enhancement as a function of the base length for a set of fabricated samples whose geometrical parameters are inside the area outlined by the white line in Figure 5. To

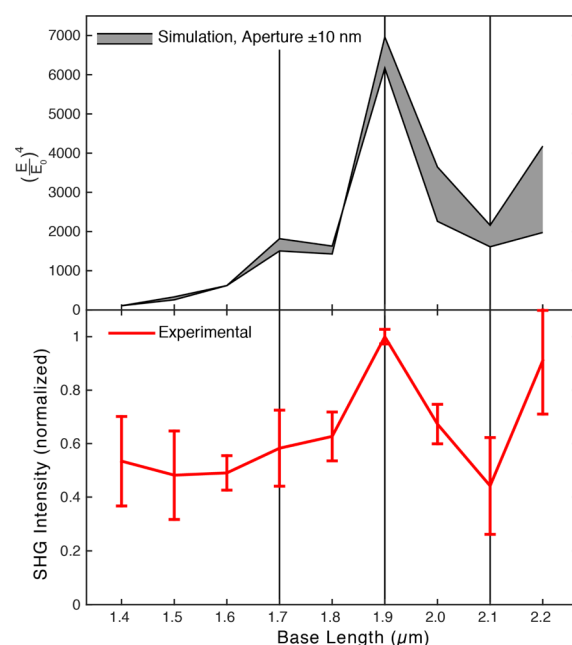


Figure 8. Comparison between experimental SH emission and FEM simulation. Experimental (red): SH signal on three sets of pyramid arrays with varying base length/aperture ranging from $1.4\text{--}2.2\text{ }\mu\text{m}$ in increments of 100 nm for the base length and from $220\text{--}340\text{ nm}$ for the aperture. Simulation (gray): result of corresponding geometries $\pm 10\text{ nm}$ for the aperture. For comparison with SH, the average field enhancement is set to the fourth power.

increase statistical significance, the experimental values are obtained by integrating three-dimensional SH intensity acquired over 28×28 pyramid arrays. Because the SH scales as I^2 , we plot the fourth power of the calculated average local-field enhancement.

The agreement in the dependence of the measured SH efficiency and the calculated enhancement on the aperture/base length is quite good, with an optimal pyramid aperture of 295 nm , which corresponds to a fabricated base length of $1.9\text{ }\mu\text{m}$. The baseline value of the normalized SH intensity is higher than the calculated values. This difference might be due to the gold roughness at the aperture, which is not taken into account in the simulations.

Since the substrate–cell interaction mechanism involves nonlinear interaction, the measured SH signal allows us to assess the potential use of the substrate in transfection experiments. Although the nonlinear order for SH is lower than the process involved in ionizing water and creating a cavitation bubble²⁰ during cell membrane poration (two versus five photons), the trends observed can be considered significant in light of our application. Given the short pulse duration produced by a fs Ti:sapphire laser and the high order of this nonlinear process, our substrates produce the intensity threshold required to generate a plasma directly in the surrounding water while reducing linear absorption and thermal damage.^{13,14}

Plasmonic nanostructures with varying pyramid baselengths (increasing size from left to right and increasing separation distance from bottom to top in Figure 9, all panels) have then been tested on a real cell poration test bench. To this end, cervix cancer cells of the HeLa line were used since they represent a well-described case model in biomedical research. The cell line was seeded directly on the substrate and then

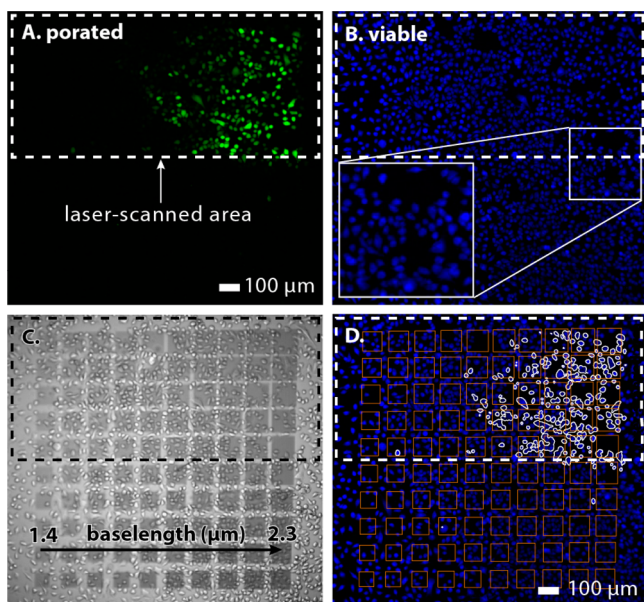


Figure 9. Demonstration of cell poration: HeLa cells cultured on a sample of tipless pyramid arrays (28×28 pyramids each) with increasing pyramid base length from left to right. The top half of the sample is laser-scanned; (A) fluorescence image. Green fluorescence indicates calcein intake by cells upon poration; (B) fluorescence image. Viable cells loaded with calcein AM red–orange (in blue), inset: closer view of outlined area; (C) bright field image; (D) composite of images from panels A, B, and C with porated cells outlined in white and pyramid arrays contour in orange.

incubated until confluency. The samples were laser raster scanned with an amplified Ti:sapphire laser ($\lambda = 800$ nm, 80 fs fwhm duration, 10 kHz repetition rate, dispersion compensated for the optical path) to induce poration. The beam diameter after focusing through a $4\times$ objective was $70 \mu\text{m}$ at the substrate, and the fluence was $6.6 \text{ mJ}/\text{cm}^2$. The substrate was scanned at a speed of $20 \text{ mm}/\text{s}$. For comparison, only the top-half of the substrate was irradiated (corresponding to the area outlined by a dashed line in each panel of Figure 9). Before irradiation, Calcein green fluorescent probe was added to the buffer to identify successfully porated cells by its intracellular intake during the process. Live cells were labeled with acetomethoxy derivate of Calcein red–orange. The fluorescence imaging was done 4 h after the laser scanning.

Figure 9, panel A shows in green successful ultrafast laser plasmonic cell poration for base length greater than $1.7 \mu\text{m}$, while keeping short-term (4 h) viability for almost all cells after irradiation (Figure 9B in blue). Figure 9, panel C is a bright-field image of the same sample area; each darker region is a 28×28 pyramids array with a defined base length and separation distance. Figure 9, panel D summarizes the information from panels A, B, and C with porated cells contour in white obtained by thresholding on the calcein fluorescence. The observed dependence of poration with respect to pyramid base length (left to right) and separation distance (bottom to top) suggests a correlation with the strength of the plasmonic effect as reported in Figures 8 and 4, respectively. However, the trend is not fully respected in the poration image where the highest concentration of porated cells seems to occur for baselengths ranging from $2\text{--}2.3 \mu\text{m}$. Similarly, we did not observe lower poration efficiency at $2.1 \mu\text{m}$. These findings suggest that other characteristics of the substrate play a role in the poration

process such as the overall pyramid size. In the time scale of the experiment, the ultrafast plasmonic poration did not affect the viability of the irradiated cells compared to nonirradiated cells. This promising poration results let us consider in-depth investigation of the poration process and its application to transfection.

In conclusion, we fabricated and characterized a plasmonic substrate based on an array of tipless pyramids for cell poration/transfection applications. We demonstrated a good agreement between simulation and two techniques (SH, NSOM) for probing the field enhancement, and explored the geometrical parameter space to identify the optimal set of parameters for strong field enhancement. Overall, the aperture and the base length are the most important geometrical parameters for enhancement at the aperture. The highest local field intensity enhancement (more than a 100-fold at 5 nm) for our tipless pyramids occurs in two sets of aperture and base length ranges: (A_p , $75\text{--}120 \text{ nm}$; BL , $1.5\text{--}2.5 \mu\text{m}$) and (A_p , $250\text{--}325 \text{ nm}$; BL , $1.75\text{--}2.5 \mu\text{m}$). Finally, this structure allowed successful plasmonic cell poration, which can be ascribed in part to the enhancement of the near-field. However, since efficient plasmonic transfection is sensitive to a manifold of processes,¹⁴ such as the heat-mediated bubbles formation, we plan further and careful investigation. Prospectively, by using photolithography rather than e-beam lithography, it is possible to fabricate a pyramid-covered surface as large as a few squared centimeters, which would allow high-throughput interaction with cell cultures and open the way to quantitative investigation of the cell transfection.

■ ASSOCIATED CONTENT

Supporting Information

A 50-fs time sequence of a FDTD simulation showing the electric field enhancement cross-section of a tipless pyramid during an excitation pulse. The Supporting Information is available free of charge on the ACS Publications website at DOI: 10.1021/acs.nanolett.5b01697.

■ AUTHOR INFORMATION

Corresponding Authors

*E-mail: Sebastien.Courvoisier@unige.ch.

*E-mail: Jean-Pierre.Wolf@unige.ch.

*E-mail: mazur@seas.harvard.edu.

Author Contributions

Several people contributed to the work described in this paper. E.D. and S.C. conceived of the basic idea for this work and optimized the fabrication method. S.C., J.C., and N.S. fabricated and imaged the samples. S.C., N.S., and M.H. designed and carried out the experimental part. M.H. took care of the simulation part with significant contribution from S.C. and J.C. M.H. and S.C. analyzed the results. L.B., J.-P.W., and E.M. supervised the research and the development of the manuscript. S.C. and J.-P.W. wrote the first draft of the manuscript; all authors subsequently took part in the revision process and approved the final copy of the manuscript.

Notes

The authors declare no competing financial interest.

■ ACKNOWLEDGMENTS

This work is based on the previous contribution of Alexander Heisterkamp, Valeria Nuzzo, and Oliver Hauser. Advice was given by Nicolas Vogel (plasmonics), Philip Muñoz (simu-

lation), and Orad Reshef (fabrication). The research described in this paper was supported by the National Science Foundation (NSF) under Contract Nos. PHY-1219334 and PHY-1205465 and by the Swiss National Foundation. Support was also given by the Ernest Boninchi foundation, AAUW Doctoral Fellowship, and HHMI International Fellowship. Facilities were provided by the Center of Nano Scale Harvard, NCCR MUST, the Aizenberg laboratory Harvard, and DPMC UNIGE.

■ REFERENCES

- (1) Nagpal, P.; Lindquist, N. C.; Oh, S.-H.; Norris, D. J. *Science* **2009**, *325*, 594–597.
- (2) Jin, Y. D. *Adv. Mater.* **2012**, *24* (38), 5153–5165.
- (3) Lindquist, N. C.; Nagpal, P.; Lesuffleur, A.; Norris, D. J.; Oh, S.-H. *Nano Lett.* **2010**, *10*, 1369–1373.
- (4) Cherukulappurath, S.; Johnson, T. W.; Lindquist, N. C.; Oh, S. H. *Nano Lett.* **2013**, *13* (11), 5635–5641.
- (5) Johnson, T. W.; Lapin, Z. J.; Beams, R.; Lindquist, N. C.; Rodrigo, S. G.; Novotny, L.; Oh, S. H. *ACS Nano* **2012**, *6* (10), 9168–9174.
- (6) Lukianova-Hleb, E. Y.; Samaniego, A. P.; Wen, J.; Metelitsa, L. S.; Chang, C.-C.; Lapotko, D. O. *J. Controlled Release* **2011**, *152*, 286–293.
- (7) Schomaker, M.; Baumgart, J.; Ngezhayay, A.; Bullerdiel, J.; Nolte, I.; Murua Escobar, H.; Lubatschowski, H.; Heisterkamp, A. *SPIE: Plasmonics Biol. Med. VI* **2009**, 7192, 71920U–71920U-8.
- (8) Baumgart, J.; Humbert, L.; Boulais, E.; Lachaine, R.; Lebrun, J.-J.; Meunier, M. *Biomaterials* **2011**, *33*, 2345–2350.
- (9) Khlebtsov, N.; Dykman, L. *Chem. Soc. Rev.* **2011**, *40*, 1647–1671.
- (10) Li, J. J.; Hartono, D.; Ong, C. N.; Bay, B. H.; Yung, L. Y. L. *Biomaterials* **2010**, *31* (23), 5996–6003.
- (11) Lee, B.; Lee, I. M.; Kim, S.; Oh, D. H.; Hesselink, L. J. *Mod. Opt.* **2010**, *57* (16), 1479–1497.
- (12) Yang, J. C.; Gao, H. W.; Suh, J. Y.; Zhou, W.; Lee, M. H.; Odom, T. W. *Nano Lett.* **2010**, *10* (8), 3173–3178.
- (13) Vogel, A.; Noack, J.; Hüttman, G.; Paltauf, G. *Appl. Phys. B: Laser Opt.* **2005**, *81* (8), 1015–1047.
- (14) Boulais, E.; Lachaine, R.; Hatef, A.; Meunier, M. *J. Photochem. Photobiol.* **2013**, *17*, 26–49.
- (15) Lindquist, N. C.; Nagpal, P.; McPeak, K. M.; Norris, D. J.; Oh, S. H. *Rep. Prog. Phys.* **2012**, *75* (3), 036501.
- (16) Sweeney, C. M.; Stender, C. L.; Nehl, C. L.; Hasan, W.; Shuford, K. L.; Odom, T. W. *Small* **2011**, *7* (14), 2032–2036.
- (17) Khoury, C. G.; Norton, S. J.; Vo-Dinh, T. *ACS Nano* **2009**, *3* (9), 2776–2788.
- (18) Kauranen, M.; Zayats, A. V. *Nat. Photonics* **2012**, *6* (11), 737–748.
- (19) Burmeister, J. S.; Olivier, L. A.; Reichert, W. M.; Truskey, G. A. *Biomaterials* **1998**, *19* (4–5), 307–325.
- (20) Schaffer, C. B.; Brodeur, A.; Mazur, E. *Meas. Sci. Technol.* **2001**, *12* (11), 1784–1794.